

Atmospheric stability sets maximum moist heat and convection in the midlatitudes

Funing Li^{a,1} and Talia Tamarin-Brodsky^a

^aDepartment of Earth, Atmospheric, and Planetary Sciences, Massachusetts Institute of Technology, Cambridge, MA 02139, USA

This manuscript was compiled on January 23, 2025

Extreme moist heatwaves pose a serious threat to society and human health. To manage heat-related risks, it is crucial to improve our understanding of what limits the maximum near-surface moist heat. This question has been extensively studied for moist heat in the tropics under the assumption of moist neutrality, but it remains less explored over midlatitude continents, where this assumption is not applicable. The frequent concurrent occurrence of extreme moist heat and intense convection over midlatitude land reinforces the prevailing hypothesis that deep convection terminates heatwaves and sets their peak intensity. Here, a theory is developed based on the onset of convection to provide a theoretical prediction for both the maximum near-surface moist heat and potential convection over midlatitude land. Our framework demonstrates that the intensities of moist heat and potential convection are constrained by a preexisting energy barrier in the lower free troposphere, which suppresses convection and enables the buildup of moist heat and convective instability. This barrier, often marked by a temperature or energy inversion, varies only slightly during moist heatwave evolution. Our results suggest the potential to predict maximum moist heat and convection from predefined lower free tropospheric properties and offer insights into the evolution of extreme heat and convection across climate states.

Moist heatwaves, which combine the effects of high temperature and humidity, pose significant risks to public health and societal outcomes (1–12). While previous research has primarily focused on the dynamics and changes of moist heat in tropical and subtropical regions (13–19), the drivers and characteristics of extreme moist heat over midlatitude continents remain poorly understood. As climate change is driving severe moist heat risks poleward into the midlatitudes (20–27), advancing our theoretical understanding of the limits of maximum moist heat in these regions has become increasingly urgent. Our goal in this study is to determine what sets the maximum moist heat over midlatitude land.

Near-surface wet bulb temperature (WBT_s) is a key measure of moist heat stress, as it combines the influence of temperature and humidity (3, 4, 16, 23, 26, 28–30). By definition, WBT represents the temperature that an air parcel would attain if cooled adiabatically to saturation at constant pressure by evaporating water into it (28, 31, 32). During this adiabatic process, the air parcel conserves its moist static energy (MSE) or the equivalent potential temperature, and thus WBT_s can be directly derived assuming the conservation of near-surface MSE (MSE_s) (15, 16, 30, 33, 34). Unlike the non-linear WBT formula, MSE is a linear function of temperature, specific humidity, and geopotential height, making it simple to use (15, 35). Accordingly, this study employs MSE_s , defined as the sum of sensible heat, latent heat, and geopotential energy at 2 meters above the ground, to measure near-surface moist heat. Overall, MSE_s reasonably represents moist heat and, similar to the annual maximum WBT_s (Fig. 1A), the annual maximum MSE_s recovers well the spatial distribution of extreme moist heat over midlatitude land (Fig. 1B) and aligns closely with WBT_s (Fig. S1; detailed in *Materials and Methods*). In this work, we use the 3-hourly ERA5 reanalysis data (36, 37) during 1980–2022 for land grids between 35°N and 75°N with elevation lower than 1000 m (detailed in *Materials and Methods*). Our analysis focuses on the annual maximum MSE_s to explore the potential constraint on the maximum moist heat over midlatitude land.

Previous studies have commonly assumed a strong coupling between the near-surface atmosphere and the free troposphere during extreme heat through deep moist convection, such that MSE_s is constrained by free tropospheric saturated moist static energy (MSE^*) given the state of convective quasi-equilibrium (3, 4, 14, 16, 38–44). Under the assumption of a moist-neutral atmospheric column, this framework has been widely used to study extreme heat in the tropics (14, 16, 18) or the global mean state (4). With the neutrality assumption, a recent study (45) has applied this framework to investigate extreme dry heat over midlatitude continents, suggesting that MSE_s is limited by 500-hPa MSE^* (i.e., $MSE_s \leq MSE_{500}^*$), thereby setting an upper bound for maximum surface air temperature. We first test the validity of this theory by comparing MSE_s with MSE_{500}^* during the annual maximum moist heat over midlatitude land. Our analysis reveals that the theory does not hold for extreme moist heat, as MSE_s is consistently and significantly greater than MSE_{500}^* in nearly all cases (more than 96% of the midlatitude land grid points; Fig. 1B–D). Furthermore, the distribution of MSE_{500}^* is largely zonally uniform (Fig. 1C), which does not capture the strong zonal variation observed in the MSE_s pattern (Fig. 1B).

These results indicate a violation of the assumption of moist neutrality because, unlike quasi-equilibrium convection in

F.L. and T.T.B. designed research and wrote the paper; F.L. performed research.

The authors declare no competing interest.

¹To whom correspondence should be addressed. E-mail: lifuning1991@gmail.com

the tropics, severe convection over midlatitude continents involves the strong storage of potential energy over a short time period (46–56), which potentially interacts with surface heat in distinct ways. Here, we propose a new theoretical framework that accounts for the onset of convection, which enables surface heat and convective instability to evolve beyond the neutral condition, and ultimately provides a tight constraint on both near-surface moist heat and potential convection over midlatitude land.

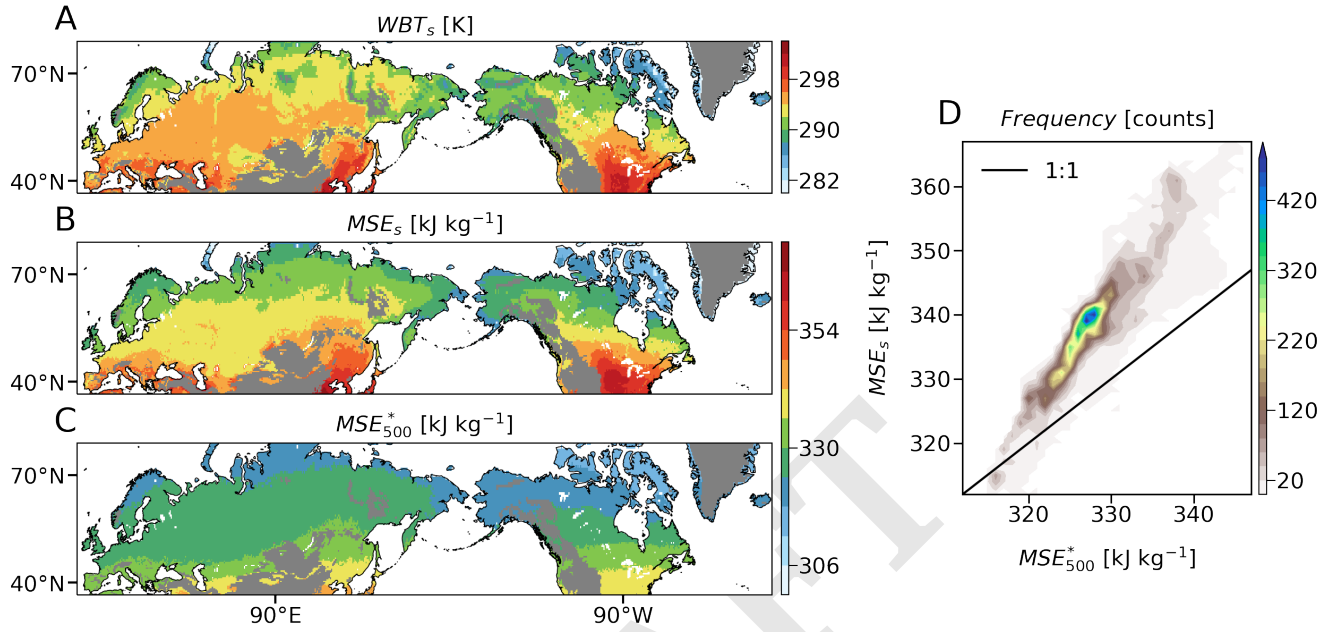


Fig. 1. Extreme moist heat. (A): Annual maximum near-surface wet-bulb temperature (WBT_s). (B): Annual maximum near-surface moist static energy (MSE_s). (C): 500-hPa saturated moist static energy (MSE_{500}^*) associated with annual maximum MSE_s . (D): Joint histogram of annual maximum MSE_s and the associated MSE_{500}^* , with a bin size of $1 \times 1 \text{ kJ kg}^{-1}$. Results are historical means based on ERA5 reanalysis data during 1980–2022 for land between 35°N and 75°N at elevations lower than 1000 m.

Concurrent moist heat and convection extremes

We first demonstrate that deep convection occurs concurrently with the annual maximum moist heat (Fig. 2), supporting the hypothesis that convective instability acts to terminate heatwaves and constrain maximum near-surface heat (4, 17, 45, 57, 58). The potential intensity of convection is measured by convective available potential energy (CAPE; detailed in *Materials and Methods*), with values of 1000 J kg^{-1} or higher typically deemed sufficient to support strong to severe convection, according to the National Weather Service guidelines (59). We define CAPE at the time of the annual maximum MSE_s as critical CAPE (denoted CAPE_c), which measures the potential convection that terminates the annual maximum moist heat. The CAPE_c over most midlatitude land regions exceeds 1000 J kg^{-1} , with values ranging from 3000 to 4000 J kg^{-1} across western Europe extending to Northeast China, and reaching 6000 J kg^{-1} or higher over eastern China and central North America (Fig. 2A). The high values of CAPE_c represent substantial convective instability in the atmosphere during extreme moist heat, indicating a significant departure from the neutrality assumption. Meanwhile, critical convective inhibition (denoted CIN_c ; detailed in *Materials and Methods*), a measure of the energy barrier in the lower free troposphere that suppresses the release of CAPE, is sufficiently low (generally less than 25 J kg^{-1}) to allow the initiation of deep free convection in the midlatitudes (Fig. S2A).

In fact, the deep convection that terminates the maximum moist heat is likely the most intense convection of the year across many midlatitude land areas, as CAPE_c (Fig. 2A) aligns closely with the annual maximum CAPE (Fig. S2B). This alignment is particularly evident in Europe and central North America, where the difference between CAPE_c and the annual maximum CAPE is less than 250 J kg^{-1} (Fig. S2C). In these regions, over 50% of the years during 1980–2022 feature simultaneous annual maxima of CAPE and MSE_s (Fig. S2C), emphasizing the frequent co-occurrence of extreme moist heat and intense convection in the midlatitudes.

Theoretical basis

CAPE scaling. We start with providing a scaling of CAPE in terms of MSE_s to demonstrate why both moist heat and potential convection maximize at the same time. Based on the definition of parcel buoyancy and simple assumptions about the geometry of CAPE, CAPE can be approximated by the difference between MSE_s and MSE_{500}^* scaled by a factor of 0.22 (detailed in

Materials and Methods):

$$CAPE \simeq 0.22(MSE_s - MSE_{500}^*). \quad [1]$$

The scaling CAPE (right hand side of Eq.1) builds a simple linear relation between CAPE and basic environmental parameters of the near-surface and free tropospheric atmospheres, without relying on the profiles of a hypothetically lifted air parcel. The scaling $CAPE_c$, estimated using MSE_s and MSE_{500}^* at the time of annual maximum MSE_s , effectively captures the spatial distribution of $CAPE_c$ (pattern correlation coefficient = 0.98; Fig. 2A and B), with values closely aligned along the one-to-one line (Fig. 2C). We assume that MSE_{500}^* remains relatively constant over short time periods, which is consistent with previous studies suggesting that the free troposphere experiences minimal variations during the heatwave evolution (45, 60) or convection build-up periods (55, 56). Consequently, based on Eq.1, CAPE and MSE_s are linearly proportional and expected to reach their peak intensities simultaneously. The frequent concurrence of extreme near-surface moist heat and convective instability suggests a shared governing process that drives the accumulation of both phenomena over midlatitude land, thereby the factor determining the maximum MSE_s simultaneously sets the maximum CAPE. We proceed to provide a theoretical prediction for both maximum moist heat and maximum potential convection.

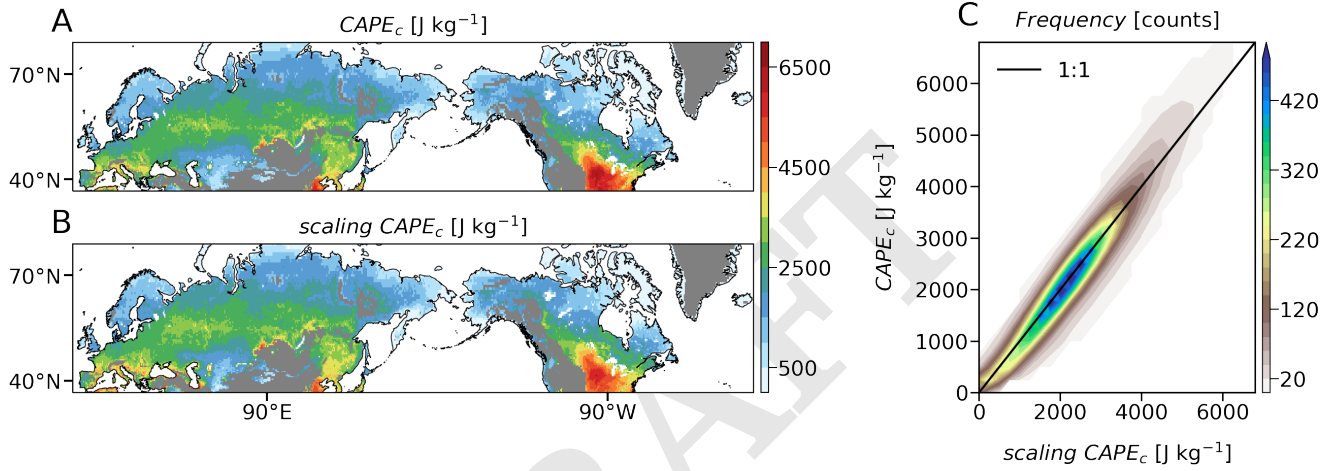


Fig. 2. Extreme convective instability. (A): Critical CAPE ($CAPE_c$), defined as CAPE at the time of annual maximum MSE_s . (B): Theoretical scaling for $CAPE_c$ following Eq.1. (C): Joint histogram of $CAPE_c$ and scaling $CAPE_c$, with a bin size of $250 \times 250 \text{ J kg}^{-1}$. Results are historical means based on ERA5 reanalysis data during 1980–2022 for land between 35°N and 75°N at elevations lower than 1000 m.

A theory for convection onset. We stick to the hypothesis that the onset of deep convection sets the maximum potential intensity of both near-surface moist heat and convection, but we incorporate a more detailed consideration of convection onset to propose a new theoretical framework. This framework allows surface heat and convective instability to evolve beyond the neutral condition, providing a tight constraint on both near-surface moist heat and convection throughout the process.

The foundation of our framework is grounded in the stored-energy nature of severe convection over midlatitude continents (46–50, 52–54), primarily attributed to a preexisting stable lower free troposphere (15, 55, 56, 61–66). For instance, as shown in a sample sounding from a week prior to the annual maximum surface moist heat in 2004 over the central United States (temperature profiles in Fig. 3A), the low-level atmospheric stability typically creates a strong layer of negative buoyancy (i.e., $b < 0$ and $CIN > 0$) that inhibits convective initiation, even when the free troposphere may already be unstable (i.e., $b > 0$ and $CAPE > 0$). Therefore, assuming sufficient heat sources, the near-surface atmosphere can continue to warm or moisten until the negative buoyancy layer is eroded, enabling the initiation of deep free convection to release CAPE and terminate the surface heat through precipitation followed by evaporative cooling. In the case study presented, near-surface heat progressively increased over the following days, accompanied by a rise in CAPE. Meanwhile, the free troposphere remained relatively constant until the time of maximum surface moist heat, when convective inhibition was nearly eliminated (temperature profiles in Fig. 3B). At the critical point, when both the MSE_s and CAPE reach their maximum values, the local atmospheric environment is characterized by $CIN_c \simeq 0$ and $CAPE_c \gg 0$ (temperature profiles in Fig. 3B), consistent with the results presented above (Fig. S2A and 2A).

Therefore, the regime of near-surface moist heat accumulation and convection buildup is constrained by $CIN \leq 0$. Since CIN essentially reflects the presence of negative buoyancy layers within the lower atmosphere, whether and when CIN approaches 0 is governed by the evolution of the most negative buoyancy ($b_{min}(z)$) throughout the low levels (55, 56). Therefore, $CIN \leq 0$ is effectively equivalent to $b_{min}(z) \leq 0$. The latter is more general and practical, as it also captures cases where CIN is 0 by definition due to the absence of a defined level of free convection (LFC) and equilibrium level (EL), with the entire atmospheric column characterized by negative buoyancy for the near-surface lifted air parcel.

As parcel buoyancy is proportional to the (virtual) temperature difference between the lifted air parcel and its environment, we further utilize the conservation of the parcel's MSE to derive an alternative formulation of temperature perturbations entirely as a function of environmental static energies (Eq.8, detailed in *Materials and Methods*). This also provides an MSE perspective to visualize the profiles of temperature perturbations and buoyancy by comparing the parcel's initial MSE (i.e., MSE_s) with the environmental moist static energy profile, which is $DSE(z) + L_v q_s$ for $z < LCL$ or $MSE^*(z)$ for $z \geq LCL$, where LCL represents the lifted condensation level (Eq.9, detailed in *Materials and Methods*). As $b_{min}(z)$ is usually above the LCL (55, 56), based on Eq.9, $b_{min}(z) \leq 0$ is equivalent to

$$b_{min}(z) \sim \min\{MSE_s - MSE^*(z)\} \leq 0 \quad [2]$$

As MSE_s does not change with height, $\min\{MSE_s - MSE^*(z)\} = MSE_s - MSE_{max}^*$, where MSE_{max}^* is the maximum MSE^* over the lower free tropospheric layers above or at LCL (detailed in *Materials and Methods*). The MSE_{max}^* quantifies the strongest energy barrier within the lower free troposphere that a near-surface air parcel must overcome to initiate convection in the absence of external forcing. Therefore, the maximum MSE_s is limited by MSE_{max}^* , such that

$$MSE_s \leq MSE_{max}^* \quad [3]$$

In addition, from the framework of scaling CAPE (Eq.1), the MSE_{max}^* and MSE_{500}^* together constrain CAPE_c by

$$CAPE_c \leq 0.22(MSE_{max}^* - MSE_{500}^*) \quad [4]$$

The right-hand side of Eqs.3 and 4 defines the maximum potential intensities of near-surface moist heat (MSE_s) and convection (CAPE), respectively. These maximum potential intensities are achievable under conditions where surface heat sources are sufficient and external lifting forces are absent, requiring $b_{min}(z)$ to approach zero to enable free convection, which is commonly observed in midlatitude continents (55, 56, 62, 67, 68). Otherwise, the actual intensities are likely to be lower than their maximum potential values.

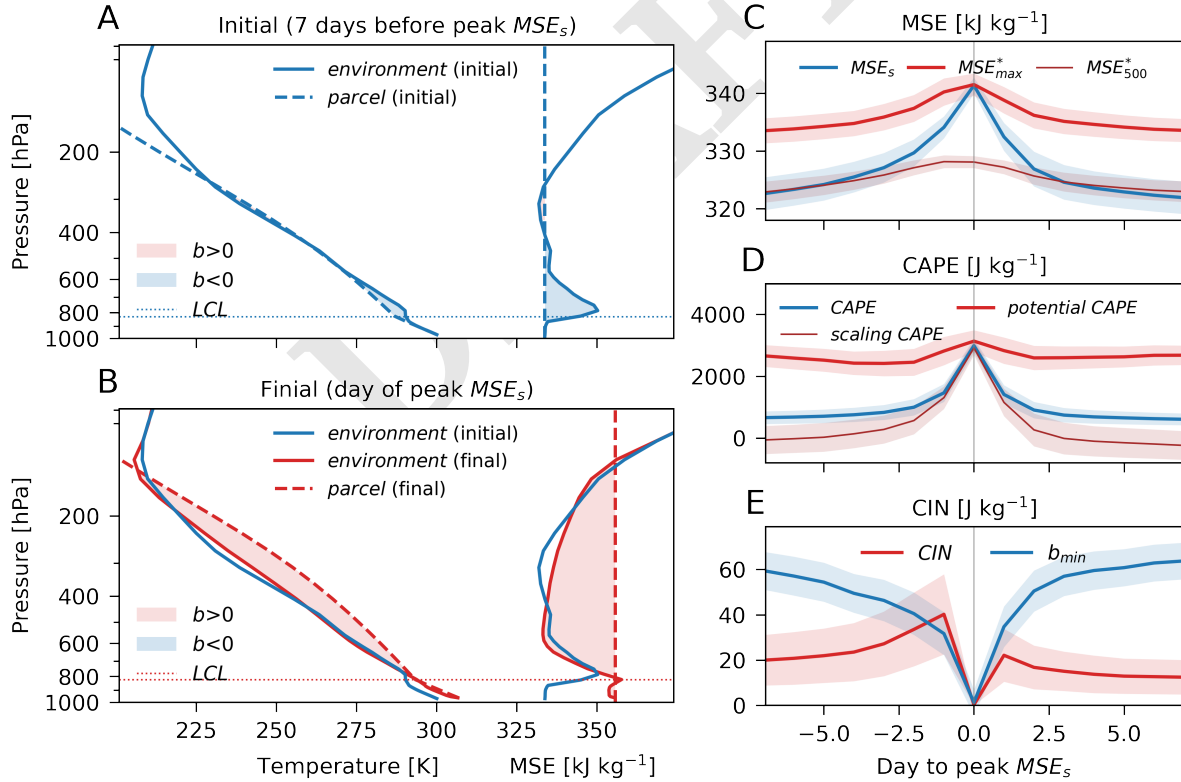


Fig. 3. Moist heat and convection buildup. (A–B): A case study associated with the annual maximum MSE_s over central United States (43°N , -97°W) in 2004, temperature sounding (left) and MSE (right) profiles for the environment (solid lines) and the air parcel (dashed lines) adiabatically lifted from the near surface, at the time of (A) 7 days before the annual maximum MSE_s and (B) the maximum MSE_s during that year. Shaded areas indicate positive ($b > 0$) and negative ($b < 0$) buoyancy, and the dotted lines represent lifted condensation level (LCL). (C–E): Composite time series, centered at the time of annual maximum MSE_s , for (C) MSE_s , MSE_{max}^* , and MSE_{500}^* ; (D) CAPE, scaling CAPE, and potential CAPE; (E) CIN and the most negative buoyancy (b_{min} , scaled by 0.005). Shading denotes \pm one standard error of the mean. The (C–E) composites are based on midlatitude continental cases where the annual maximum MSE_s and CAPE occur concurrently, with $CAPE_c > 500 \text{ J kg}^{-1}$, $CIN_c < 5 \text{ J kg}^{-1}$, and the maximum CIN within 7 days before the peak heat of at least 50 J kg^{-1} (detailed in *Materials and Methods*). Results are based on ERA5 reanalysis data.

Maximum potential moist heat and convection

We first present the results of the sounding evolutions for the case discussed above, analyzed within the developed MSE framework. As a validation of Eq.9, the MSE profiles (Fig. 3A and B) recover well the positive and negative buoyancy layers and their temporal evolutions. Compared to temperature profiles, the MSE profiles more clearly delineate the most negative buoyancy layer prior to the annual maximum moist heat, identified by a distinct MSE* inversion above the LCL (Fig. 3A). The preexisting MSE*_{max} resides at the peak of the MSE* inversion near 800 hPa (MSE profiles in Fig. 3A), and eventually aligns with the LCL (MSE profiles in Fig. 3B). In this case, the final MSE*_{max} effectively sets the maximum MSE_s achieved at the time of the annual maximum moist heat, when b_{min} (and hence CIN_c) approaches 0 and CAPE_c is maximized. Relative to the significant changes in MSE_s during this period, the preexisting MSE*_{max} intensities only slightly over time, which suggests the possibility of predicting the maximum potential intensity of MSE_s (and consequently CAPE_c) based on the initial MSE*_{max}, although adjustments are needed over time as MSE*_{max} evolves.

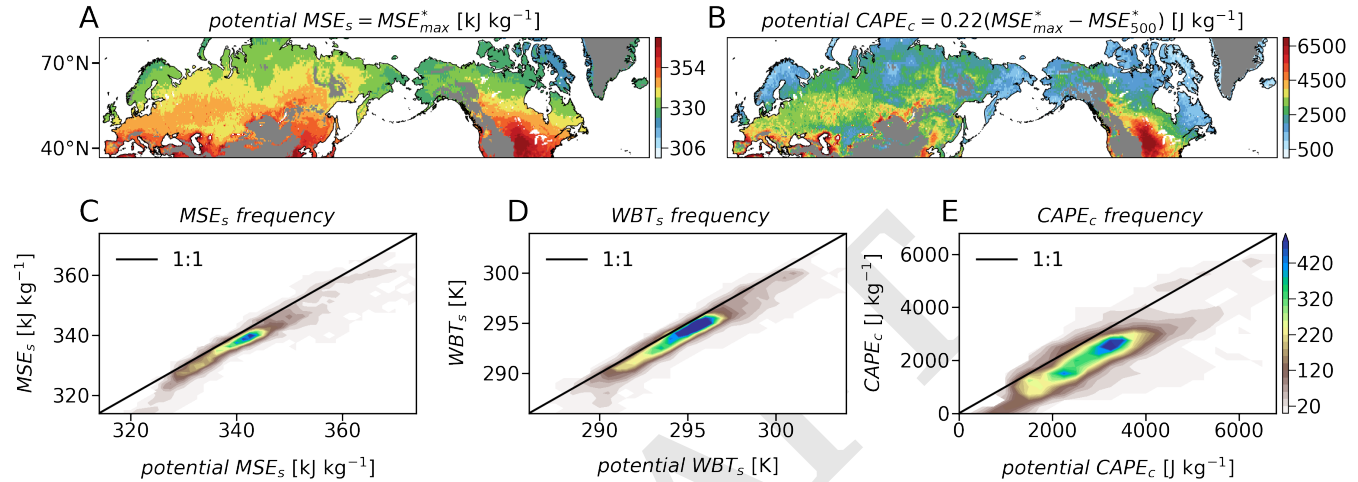


Fig. 4. Maximum potential moist heat and convection. (A): Annual maximum potential MSE_s , defined as MSE_{max}^* corresponding to the maximum MSE_s following Eq.3. (B): Annual maximum potential $CAPE_c$, defined by CAPE scaling based on MSE_{max}^* and MSE_{500}^* following Eq.4. (C–E): Joint histograms of (C) annual maximum MSE_s and the potential intensity with a bin size of $1.25 \times 1.25 \text{ kJ kg}^{-1}$, (D) annual maximum WBT_s and the potential intensity with a bin size of $0.5 \times 0.5 \text{ K}$, and (E) $CAPE_c$ and the potential intensity with a bin size of $250 \times 250 \text{ J kg}^{-1}$. Results are historical means based on ERA5 reanalysis data during 1980–2022 for land between 35°N and 75°N at elevations lower than 1000 m.

To evaluate the generality of the above results, we extend the analysis by presenting composite time series of key proxies derived from a subset of cases over midlatitude land. Specifically, we focus on instances of concurrent annual maxima in MSE_s and CAPE for each year during 1980–2022 (44.5% of all cases; Fig. S2D). To best visualize the features aligning with our theoretical framework - where MSE_s and CAPE are maximized as preexisting CIN is eroded to zero - we further select cases based on the following criteria: $CAPE_c > 500 \text{ J kg}^{-1}$, $CIN_c \leq 0$, and a maximum CIN of at least 50 J kg^{-1} within seven days preceding the critical time (detailed in *Materials and Methods*). These selection criteria yield 2502 cases per year (27% of concurrent cases), for which we plot composite 14-day time series centered on the time of maximum MSE_s (Fig. 3C–E). Following the maximum potential for moist heat defined by Eq.3, MSE_s increases over time and ultimately converges toward MSE_{max}^* at the peak time (Fig. 3C). The height of MSE_{max}^* is in general between 750–800 hPa, and decreases gradually with time to approach LCL (Fig. S3). Notably, MSE_{500}^* fails to predict the maximum MSE_s as discussed above, as MSE_s exceeds MSE_{500}^* as early as seven days before the peak, with the difference rapidly amplifying over time (Fig. 3C). This growing discrepancy between MSE_s and MSE_{500}^* reflects the progressive accumulation of CAPE leading up to the peak, as recovered by the scaling CAPE following Eq.1 and constrained by the maximum potential for convection defined in Eq.4 (Fig. 3D). Fundamentally, the composite temporal evolutions of MSEs and CAPE are linked to the removal of CIN or b_{min} (Fig. 3E), supporting our basic hypothesis formulated in Eq.2. These results are broadly consistent when we perform composite analyses based on all cases of concurrent moist heat and convection over midlatitude land (detailed in *Materials and Methods*; Fig. S4), though the maximum potential intensities of MSE_s and CAPE_c are not necessarily achieved (Fig. S4A–B). This suggests the potential influence of external forcing mechanisms of lift (69–71), which may facilitate the initiation of convection in cases with non-zero CIN_c (Fig. S4C). Similarly, the composite results reveal relatively steady time series for MSE_{max}^* and MSE_{500}^* (Fig. 3C), as well as for the potential CAPE (Fig. 3D), highlighting the potential to predict the maximum intensities of MSE_s and CAPE based on preexisting free tropospheric properties.

Lastly, to comprehensively validate the maximum potential intensity framework (i.e., Eqs.3 and 4), we compare the observed annual maximum moist heat (MSE_s) and the associated critical convection (CAPE_c) with their potential maxima derived for all cases over midlatitude land during 1980–2022 from the ERA5 reanalysis data (Fig. 4). Here, MSE_{max}^* and MSE_{500}^* are calculated at the time of annual maximum MSE_s. Overall, the maximum potential MSE_s (Fig. 4A) and the maximum

potential CAPE_c (Fig. 4B) capture the spatial patterns of the observed maximum MSE_s (Fig. 1B) and CAPE_c (Fig. 2A) over midlatitude land, with observed maxima slightly smaller than their potential counterparts. The pattern correlation coefficient is 0.94 between observed and potential MSE_s maxima, and 0.82 between observed and potential CAPE_c. The joint histograms of all cases further confirm that the maximum potential intensities serve as a tight upper limit for the observed maximum MSE_s and CAPE_c (Fig. 4C and E). For the maximum MSE_s, the potential MSE_s is achievable for many cases, with others closely aligned with the one-to-one line but slightly below (Fig. 4C). Translating (potential) MSE_s into (potential) WBT_s (as detailed in Materials and Methods) yields consistent results (Fig. 4D), highlighting the applicability of our theory for directly predicting maximum WBT_s. Similarly, the potential CAPE_c serves as a strong constraint on the observed CAPE_c (Fig. 4E), although the actual CAPE_c exhibits greater variability for a given potential CAPE_c, partly due to the variations in MSE_s.

Conclusion and discussion

This study proposed a theoretical prediction for maximum potential moist heat (MSE_s) and convection (CAPE) over midlatitude land, both tightly constrained by a preexisting energy (MSE^{*}) inversion within the lower free troposphere. The maximum MSE^{*} at the energy inversion layer (i.e., MSE_{max}^{*}) acts as a substantial energy barrier that suppresses the free convection of near-surface air parcels, thereby allowing the warming or moistening of near-surface air and the accumulation of convective instability. This process continues until MSE_s reaches MSE_{max}^{*}, such that the near-surface air parcels are sufficiently energetic to overcome the energy barrier, initiate deep free convection, and terminate surface heating. This theory does not address the mechanisms by which moist heat or convective instability increases, which may be driven by various physical processes (e.g., warm advection, adiabatic warming in subsiding air, or diabatic heating from surface fluxes and radiation) associated with large-scale dynamics such as storm tracks or atmospheric blockings (30, 56, 60, 72–80). Instead, it focuses on quantifying the upper limit of these increases before free convection is triggered, assuming sufficient heating sources.

A recent study examined a similar topic over midlatitude continents, but focusing on extreme dry heat under the assumption of moist neutrality (45), and suggested that 500-hPa MSE₅₀₀^{*} acts as an upper bound for MSE_s. However, we have shown that this assumption fails for extreme moist heat over midlatitude land. In fact, the neutrality assumption also breaks down for extreme dry heat in the midlatitudes, as MSE_s exceeds MSE₅₀₀^{*} in most cases of annual maximum surface air temperature (Fig. S5A). Our CAPE scaling framework (Eq. 1) reveals that MSE₅₀₀^{*} generally approximates the minimum energy of the free troposphere (detailed in *Materials and Methods*), and the surplus of MSE_s over MSE₅₀₀^{*} effectively defines the accumulated convective instability beyond moist neutrality. When applied to extreme dry heat conditions, our theory also predicts well the maximum potential intensities of MSE_s and CAPE_c during extreme dry heat periods (Fig. S5B–C), thereby generalizing our theory and highlighting the critical role of preexisting low-level energy inversions in setting near-surface maximum heat.

Our study advances previous work by carefully addressing the onset of convection, demonstrating how the atmosphere evolves beyond the neutral condition – where parcel buoyancy and CAPE are zero by definition – in alignment with the stored-energy nature of severe convection in the midlatitudes (46–56). Future work could incorporate other processes (e.g., wind shear (81–83), entrainments (17, 42, 84), and external forcings (69–71, 83, 85–89)) to more precisely determine the onset of convection and, consequently, the termination of heatwaves. For example, a recent study highlighted the critical role of dry air entrainment in suppressing deep convection and intensifying moist heat in tropical and subtropical regions (17), though the entrainment influence may vary strongly with the severity of convection in midlatitude due to the dependence on vertical wind shear (90, 91).

The preexisting MSE^{*} inversion within the lower free troposphere is typically marked by a pronounced temperature inversion or a layer where the temperature decreases most gradually with height (15, 55, 56, 61–66). While this study proposed the theoretical framework based on evolution of local convective instability, the formation of preexisting inversion layers might be non-local due to advection of a warm layer from an adjacent region or the adiabatically warmed air from the subsidence of large-scale circulation (e.g., anticyclones) (15, 56, 61, 65, 92). Thus, it might be worthwhile to investigate the origins and evolutions of the inversion layers from the Lagrangian perspective (55, 56, 74, 76, 93, 94) to provide insight into the formation and potential magnitude of MSE_{max}^{*}, and thus improve the predictability of local potential moist heat and convection. This is also critical for understanding the role of preexisting lower free tropospheric inversion layers in future climates, as shifts in land cover or regionally uneven warming could affect the formation and transport pathways of inversion layers between regions (53, 56, 66, 95–98), thereby potentially shaping future spatial patterns of extreme heat and convection (26, 99–101).

Materials and Methods

Data. We use 3-hourly near-surface and pressure-level ERA5 reanalysis data with a horizontal grid spacing of 0.5° latitude by 0.5° longitude during 1980–2022 (36, 37), for land grid points between 35°N and 75°N at elevations lower than 1000 m (20854 grid points per year in total). ERA5 reanalysis data are widely used in studies of global temperature extremes and convective environments, as they accurately capture observed temperature and moisture profiles in general (56, 102, 103), including inversion features within the lower free troposphere (64, 66). In this study, calculations for all variables are initially performed at the 3-hourly interval and then sampled based on the daily maximum MSE_s to create a dataset of daily maximum moist heat. Our analyses focus on the annual maximum moist heat, obtained by further sampling the dataset given the annual maximum MSE_s at each grid point for each year. This process yields 43 samples per land grid point, corresponding to the maximum MSE_s for each year during 1980–2022. For analyses related to extreme near-surface dry heat, the data are generated in the same manner but are conditioned on the maximum near-surface dry heat, defined as the maximum 2-m air temperature (T_s).

MSE and WBT. MSE is defined as the sum of sensible heat ($c_p T$), latent heat ($L_v q$), and geopotential energy (gz), i.e., $MSE = c_p T + L_v q + gz$, where $c_p = 1005 \text{ J kg}^{-1} \text{ K}^{-1}$ is the specific heat capacity of air at constant pressure, $L_v = 2.5 \times 10^6 \text{ J kg}^{-1}$ is the latent heat of vaporization, $g = 9.81 \text{ m s}^{-2}$ is gravitational acceleration, T is air temperature, q is specific humidity, and z is height above sea level (47). Near-surface (denoted by subscript “ s ”) MSE, MSE_s , is calculated using quantities at 2-m above ground surface, where the geopotential height equals to 2 plus the surface elevation in meters. Saturated (denoted by superscript “ $*$ ”) MSE, MSE^* , is calculated by replacing q with the saturated specific humidity (q^*), which is a function of air temperature and pressure. In an adiabatic process, MSE is generally considered a conserved quantity given hydrostatic balance (47, 104, 105), interconvertible with equivalent potential temperature (35, 106, 107). As a part of MSE, dry static energy (DSE) is the sum of $c_p T$ and gz , which is conserved under dry adiabatic conditions and is thermodynamically equivalent to potential temperature (47, 108). MSE_{max}^* is identified as the maximum MSE^* within the lower free troposphere, specifically at or above LCL but below 300 hPa.

WBT_s is calculated based on the conversion of MSE_s (16, 109). Specifically, for each MSE_s , we solve the equation $MSE_s = c_p WBT_s + L_v q^*(WBT_s, p_s) + gz_s$ for the corresponding WBT_s , where $q^*(WBT_s, p_s)$ is the saturated specific humidity at temperature WBT_s and surface pressure p_s . As $q^*(WBT_s, p_s)$ is proportional with WBT_s based on the Clausius–Clapeyron scaling (110), WBT_s exhibits a nearly one-to-one relationship with MSE_s (Fig. S1) (15, 16). There is a small variation in WBT_s given a value of MSE_s , due to dependence on the elevation variance (0–1000 m; Fig. S1). Similarly, we calculate the maximum potential WBT_s (Fig. 4D) by solving WBT_s from the equation $MSE_{max}^* = c_p WBT_s + L_v q^*(WBT_s, p_s) + gz_s$ at the time of annual maximum MSE_s .

Composite time series. Composite time series analyses (Fig. 3C–E) are based on a subset of extreme moist heat and convection cases. To focus on the locally most extreme moist cases, we first select cases of annual maximum MSE_s when its $CAPE_c$ corresponds to the local annual maximum CAPE (i.e., cases with moist heat and convection both maximized at the same time during the year). This step on average yields 9270 cases per year (i.e., 44.5% of all cases), with mean CAPE of up to 3011 J kg^{-1} and mean CIN as low as 12 J kg^{-1} . There are a few cases over far northern Canada (Nunavut area), where convection is rare and the annual maximum CAPE is less than 500 J kg^{-1} . Thus, those cases with $CAPE_c \leq 500 \text{ J kg}^{-1}$ are excluded, which further yields 8959 cases per year. Composite time series based on this large group of cases is shown in Fig. S4. The composite time series indicates a substantial increase of MSE_s bounded by MSE_{max}^* (Fig. S4A) and the buildup of CAPE bounded by the potential CAPE (Fig. S4B), along with the removal of the most negative buoyancy (Fig. S4C). These results are broadly consistent with that shown in main text (Fig. 3C–E).

We further select cases where the theoretical maximum potential intensities (Eqs. 3–4) are likely achieved and the preexisting energy barrier is relatively large, by conditioning on $CIN_c \leq 5 \text{ J kg}^{-1}$ and the maximum CIN of at least 50 J kg^{-1} within 7 days preceding the critical time. This leads to 2502 cases per year (i.e., 12% of all cases), with the composite time series shown in the main text (Fig. 3C–E).

Parcel buoyancy and temperature perturbation. To link surface moist heat with convection, we begin by deriving an expression for parcel buoyancy as a function of near-surface moist static energy.

Considering an undiluted air parcel adiabatically lifted upward from the near-surface (2 m above ground surface; denoted by subscript “ s ” in derivations) and neglecting the relatively small contribution to density changes due to pressure perturbation and virtual temperature correction (47, 111), the parcel buoyancy at a given height z ($b(z)$) is proportional to differences in sensible heat between the air parcel and the environment ($c_p \Delta T(z)$), where $\Delta T(z) = T_a(z) - T(z)$ is temperature perturbations of the air parcel ($T_a(z)$, with subscript “ a ” referring to the air parcel) with respect to the environment ($T(z)$) and $c_p = 1005 \text{ J kg}^{-1} \text{ K}^{-1}$ is the specific heat capacity of air at constant pressure. During an adiabatic process, it is common to assume that the air parcel conserves its moist static energy such that $MSE_a(z) = MSE_s$. Therefore, the vertical profile of $b(z)$ or $c_p \Delta T(z)$ is given by

$$b(z) \sim c_p \Delta T(z) = MSE_s - DSE(z) - L_v q_a(z) \quad [5]$$

where $DSE(z)$ is vertical profile of the environmental dry static energy.

To derive parcel buoyancy solely as a function of environmental parameters, independent of the lifted air parcel’s profiles, the specific humidity of the air parcel ($q_a(z)$) in Eq. 5 can be further approximated using environmental parameters that vary with height (z) relative to the lifted condensation level (LCL).

For $z < LCL$, the air parcel remains unsaturated and maintains its specific humidity at the initial value. Hence,

$$q_a(z) = q_s \quad [6]$$

For $z \geq LCL$, the air parcel is saturated, such that the parcel specific humidity equals its saturated specific humidity ($q_a^*(z)$, with superscript “ $*$ ” referring to a quantity at saturation), which is a function of the parcel temperature and air pressure. As pressure difference between the air parcel and environment is negligible (47, 111), the difference in saturated specific humidity between the air parcel and environment is caused by difference in temperature, and thus $q_a^*(z)$ can be written as a linear relation to the environmental saturated specific humidity ($q^*(z)$) via $q_a^*(z) = q^*(z) + (\partial q^*(z)/\partial T(z)) \Delta T(z)$. We further assume constant $\partial q^*(z)/\partial T(z)$ and approximate it by $L_v q^*(z)/(R_v T^2(z))$ using Clausius–Clapeyron equation, where $R_v = 461 \text{ J kg}^{-1} \text{ K}^{-1}$ is gas constant for water vapor. Hence,

$$q_a(z) = q_a^*(z) \simeq q^*(z) + \frac{L_v q^*(z)}{R_v T^2(z)} \Delta T(z) \quad [7]$$

Substituting Eqs. 6 and 7 into Eq. 5 and rearranging it gives

$$b(z) \sim c_p \Delta T(z) \simeq \begin{cases} DSE_s - DSE(z), & z < LCL \\ \frac{MSE_s - MSE^*(z)}{1 + \frac{L_v^2 q^*(z)}{c_p R_v T^2(z)}}, & z \geq LCL \end{cases} \quad [8]$$

Eq. 8 recovers the vertical profiles of temperature perturbations (Fig. S6A). The denominator $1 + L_v^2 q^*(z)/(c_p R_v T^2(z))$ is always positive, ranging from ~ 3 in the lower free troposphere above the LCL to ~ 1 in the upper free troposphere (Fig. S6B), which does not alter the sign of buoyancy across the atmospheric column or the location of the most negative buoyancy within the lower free troposphere (Fig. S6A). Therefore, Eq. 8 is further simplified in a scaling format,

$$b(z) \sim c_p \Delta T(z) \sim \begin{cases} MSE_s - (DSE(z) + L_v q_s), & z < LCL \\ MSE_s - MSE^*(z), & z \geq LCL \end{cases} \quad [9]$$

Eq. 9 provides an alternative approach to quantify temperature perturbation profile from the MSE prospective (a more precise form is given by Eq. 8; Fig. S6A). This eliminates the need to first calculate the temperature profile of a hypothetically lifted air parcel.

Instead, the vertical profile of parcel buoyancy can be determined directly by comparing the parcel's initial MSE (i.e., MSE_s) with the environmental static energy profile ($DSE(z) + L_v q_s$ if $z < LCL$ or $MSE^*(z)$ if $z \geq LCL$). Furthermore, this approach is equivalent to comparing near-surface potential temperature with the potential temperature profile for $z < LCL$ or the near-surface equivalent potential temperature with the saturation equivalent potential temperature profile for $z \geq LCL$.

CAPE and scaling CAPE. We calculate convective available potential energy (CAPE) for the near-surface air parcel by integrating virtual temperature difference between the air parcel ($T_{v,a}$) and environment (T_v) with respect to natural logarithm of pressure ($\ln p$) from the level of free convection (LFC) to equilibrium level (EL), given by

$$CAPE = -R_d \int_{p_{LFC}}^{p_{EL}} \Delta T_v d\ln p \quad [10]$$

where $\Delta T_v = T_{v,a} - T_v$, $R_d = 287 \text{ J kg}^{-1} \text{ K}^{-1}$ is the ideal gas constant of dry air, p_{LFC} and p_{EL} are pressure at LFC and EL, respectively. Moist adiabats for the air parcel follow irreversible pseudoadiabatic process (112). This makes little differences as compared to reversible process (113). Based on ideal gas law, Eq.10 is equivalent to the integral of parcel buoyancy with respect to height. The convective inhibition (CIN) is calculated in the same way as CAPE but for negative buoyancy from the surface to LFC. In this work, CIN is defined as positive by its absolute value.

Next, we derive a scaling for CAPE from Eq.10 combining simple assumptions. Since ΔT_v is zero at both LFC and EL and reaches its maximum approximately midway between these levels ($\sim 500 \text{ hPa}$, typically above LCL at the height of minimum MSE^* ; Fig. S3), CAPE can be geometrically approximated as the area of a triangle with $-R_d \int_{p_{LFC}}^{p_{EL}} d\ln p = R_d \ln(p_{LFC}/p_{EL})$ being the base and ΔT_v at 500 hPa ($\Delta T_{v,500}$, with superscript "500" referring to a quantity at 500 hPa) being the height. Further neglecting virtual temperature correction (i.e., $\Delta T_{v,500} \simeq \Delta T_{500}$) and substituting Eq.8, we have that

$$CAPE \simeq \frac{R_d \ln(p_{LFC}/p_{EL})}{2c_p} \frac{MSE_s - MSE_{500}^*}{1 + \frac{L_v^2 q_{500}^*}{c_p R_v T_{500}^2}} \quad [11]$$

Here we focus on midlatitude extreme moist heat conditions where CAPE is in general high ($>1000 \text{ J kg}^{-1}$). For those cases, the LFC is near the lower free troposphere and EL is close to the tropopause, and we approximate them by $p_{LFC} \simeq 950 \text{ hPa}$ and $p_{EL} \simeq 100 \text{ hPa}$. The mean $T_{500} \simeq 260 \text{ K}$ gives $q_{500}^* \simeq 0.0028 \text{ kg kg}^{-1}$. Substituting these typical values into Eq.11, we provide a scaling for midlatitude high CAPE:

$$CAPE \simeq 0.22(MSE_s - MSE_{500}^*) \quad [12]$$

Previous studies have explored the relationship between CAPE and environmental MSE, either under the radiative–convective equilibrium framework (52, 114, 115) or through linear regression methods (116). In contrast, our derivation begins with the fundamental definitions of parcel buoyancy and CAPE, similar to (117) but incorporating minimal assumptions about the geometric characteristics of CAPE, to establish a robust linear relationship between CAPE and key atmospheric parameters near the surface and in the free troposphere. The coefficient in Eq.12 may vary with p_{LFC} , p_{EL} , and T_{500} , which can be precisely adjusted using the full scaling equation (Eq.11) when applied to different regions or datasets. Here, the derived coefficient of 0.22 for high-CAPE environments over midlatitude land aligns closely with the linear regression results (0.22–0.29) reported for high CAPE over continental North America (116).

Data Availability. The 3-hourly ERA5 reanalysis data (36, 37) from 1980–2022 are publicly available at <https://rda.ucar.edu/datasets/ds633.0/>.

Code Availability. The xcape python package is available at <https://github.com/xgcm/xcape/tree/master>. The Metpy python package is available at <https://unidata.github.io/MetPy/latest/index.html>.

ACKNOWLEDGMENTS. This research is part of the MIT Climate Grand Challenge on Weather and Climate Extremes. Support was provided by Schmidt Sciences, LLC. We thank Kerry Emanuel, Paul O'Gorman, P. J. Tuckman, and Divya Rea for helpful discussions.

1. R Basu, JM Samet, Relation between elevated ambient temperature and mortality: a review of the epidemiologic evidence. *Epidemiol. reviews* **24**, 190–202 (2002).
2. R Basu, High ambient temperature and mortality: a review of epidemiologic studies from 2001 to 2008. *Environ. health* **8**, 1–13 (2009).
3. SC Sherwood, M Huber, An adaptability limit to climate change due to heat stress. *Proc. Natl. Acad. Sci.* **107**, 9552–9555 (2010).
4. JR Buzan, M Huber, Moist heat stress on a hotter earth. *Annu. Rev. Earth Planet. Sci.* **48**, 623–655 (2020).
5. CZ De Lima, et al., Heat stress on agricultural workers exacerbates crop impacts of climate change. *Environ. Res. Lett.* **16**, 044020 (2021).
6. Q Kong, M Huber, Explicit calculations of wet-bulb globe temperature compared with approximations and why it matters for labor productivity. *Earth's Futur.* **10**, e2021EF002334 (2022).
7. C Lesk, et al., Compound heat and moisture extreme impacts on global crop yields under climate change. *Nat. Rev. Earth & Environ.* **3**, 872–889 (2022).
8. W Saeed, et al., The poverty impacts of labor heat stress in west africa under a warming climate. *Earth's Futur.* **10**, e2022EF002777 (2022).
9. JW Baldwin, et al., Humidity's role in heat-related health outcomes: a heated debate. *Environ. health perspectives* **131**, 055001 (2023).
10. J Vanos, et al., A physiological approach for assessing human survivability and liveability to heat in a changing climate. *Nat. communications* **14**, 7653 (2023).
11. CD Diaz, et al., Increased extreme humid heat hazard faced by agricultural workers. *Environ. Res. Commun.* **5**, 115013 (2023).
12. Q Guo, et al., Regional variation in the role of humidity on city-level heat-related mortality. *PNAS nexus* **3**, pgae290 (2024).
13. V Mishra, et al., Moist heat stress extremes in india enhanced by irrigation. *Nat. Geosci.* **13**, 722–728 (2020).
14. MP Byrne, Amplified warming of extreme temperatures over tropical land. *Nat. Geosci.* **14**, 837–841 (2021).
15. C Raymond, et al., On the controlling factors for globally extreme humid heat. *Geophys. Res. Lett.* **48**, e2021GL096082 (2021).
16. Y Zhang, I Held, S Fueglister, Projections of tropical heat stress constrained by atmospheric dynamics. *Nat. Geosci.* **14**, 133–137 (2021).
17. SQ Duan, F Ahmed, JD Neelin, Moist heatwaves intensified by entrainment of dry air that limits deep convection. *Nat. Geosci.* **17**, 837–844 (2024).
18. Y Zhang, WR Boos, I Held, CJ Paciorek, S Fueglister, Forecasting tropical annual maximum wet-bulb temperatures months in advance from the current state of enso. *Geophys. Res. Lett.* **51**, e2023GL106990 (2024).
19. SQ Duan, KA McKinnon, IR Simpson, Two perspectives on amplified warming over tropical land examined in cmip6 models. *J. Clim.* (2024).
20. TK Matthews, RL Wilby, C Murphy, Communicating the deadly consequences of global warming for human heat stress. *Proc. Natl. Acad. Sci.* **114**, 3861–3866 (2017).
21. ED Coffel, RM Horton, A De Sherbinin, Temperature and humidity based projections of a rapid rise in global heat stress exposure during the 21st century. *Environ. Res. Lett.* **13**, 014001 (2017).
22. C Tuholtske, et al., Global urban population exposure to extreme heat. *Proc. Natl. Acad. Sci.* **118**, e2024792118 (2021).
23. C Raymond, T Matthews, RM Horton, The emergence of heat and humidity too severe for human tolerance. *Sci. Adv.* **6**, eaaw1838 (2020).
24. CD Rogers, et al., Recent increases in exposure to extreme humid-heat events disproportionately affect populated regions. *Geophys. Res. Lett.* **48**, e2021GL094183 (2021).
25. DM Romps, YC Lu, Chronically underestimated: a reassessment of us heat waves using the extended heat index. *Environ. Res. Lett.* **17**, 094017 (2022).
26. DJ Vecellio, Q Kong, WL Kenney, M Huber, Greatly enhanced risk to humans as a consequence of empirically determined lower moist heat stress tolerance. *Proc. Natl. Acad. Sci.* **120**, e2305427120 (2023).
27. K Zhang, et al., Increased heat risk in wet climate induced by urban humid heat. *Nature* **617**, 738–742 (2023).

28. J Haldane, The influence of high air temperatures no. i. *Epidemiol. & Infect.* **5**, 494–513 (1905).

29. J Buzan, K Oleson, M Huber, Implementation and comparison of a suite of heat stress metrics within the community land model version 4.5. *Geosci. Model. Dev.* **8**, 151–170 (2015).

30. Q Kong, M Huber, Regimes of soil moisture–wet-bulb temperature coupling with relevance to moist heat stress. *J. Clim.* **36**, 7925–7942 (2023).

31. R Davies-Jones, An efficient and accurate method for computing the wet-bulb temperature along pseudoadiabats. *Mon. Weather. Rev.* **136**, 2764–2785 (2008).

32. R Stull, Wet-bulb temperature from relative humidity and air temperature. *J. applied meteorology climatology* **50**, 2267–2269 (2011).

33. EM Fischer, R Knutti, Robust projections of combined humidity and temperature extremes. *Nat. Clim. Chang.* **3**, 126–130 (2013).

34. CC Ivanovich, AH Sobel, RM Horton, C Raymond, Stickiness: A new variable to characterize the temperature and humidity contributions toward humid heat. *J. Atmospheric Sci.* **81**, 819–837 (2024).

35. DR Chavas, J Peters, Static energy deserves greater emphasis in the meteorology community. *Bull. Am. Meteorol. Soc.* **104**, E1918–E1927 (2023).

36. European Centre for Medium-Range Weather Forecasts, ERA5 Reanalysis (0.25 Degree Latitude-Longitude Grid) (2019).

37. H Hersbach, et al., The ERA5 global reanalysis. *Q. J. Royal Meteorol. Soc.* **146**, 1999–2049 (2020).

38. KA Emanuel, J David Neelin, CS Bretherton, On large-scale circulations in convecting atmospheres. *Q. J. Royal Meteorol. Soc.* **120**, 1111–1143 (1994).

39. JD Neelin, N Zeng, A quasi-equilibrium tropical circulation model—formulation. *J. atmospheric sciences* **57**, 1741–1766 (2000).

40. IN Williams, RT Pierrehumbert, M Huber, Global warming, convective threshold and false thermometers. *Geophys. Res. Lett.* **36** (2009).

41. MP Byrne, PA O’Gorman, Land–ocean warming contrast over a wide range of climates: Convective quasi-equilibrium theory and idealized simulations. *J. Clim.* **26**, 4000–4016 (2013).

42. MS Singh, PA O’Gorman, Influence of entrainment on the thermal stratification in simulations of radiative-convective equilibrium. *Geophys. Res. Lett.* **40**, 4398–4403 (2013).

43. RA Zamora, RL Korty, M Huber, Thermal stratification in simulations of warm climates: A climatology using saturation potential vorticity. *J. Clim.* **29**, 5083–5102 (2016).

44. Y Zhang, S Fueglistaler, How tropical convection couples high moist static energy over land and ocean. *Geophys. Res. Lett.* **47**, e2019GL086387 (2020).

45. Y Zhang, WR Boos, An upper bound for extreme temperatures over midlatitude land. *Proc. Natl. Acad. Sci.* **120**, e2215278120 (2023).

46. CA Doswell III, The distinction between large-scale and mesoscale contribution to severe convection: A case study example. *Weather. Forecast.* **2**, 3–16 (1987).

47. K Emanuel, *Atmospheric Convection*. (Oxford University Press, USA), (1994).

48. CA Doswell, Severe convective storms—an overview in *Severe convective storms*. (Springer), pp. 1–26 (2001).

49. JP Chaboureau, F Guichard, JL Redelsperger, JP Lafore, The role of stability and moisture in the diurnal cycle of convection over land. *Q. J. Royal Meteorol. Soc.* **130**, 3105–3117 (2004).

50. P Bechtold, et al., The simulation of the diurnal cycle of convective precipitation over land in a global model. *Q. J. Royal Meteorol. Soc.* **130**, 3119–3137 (2004).

51. EJ Zipser, DJ Cecil, C Liu, SW Nesbitt, DP Yorty, Where are the most intense thunderstorms on earth? *Bull. Am. Meteorol. Soc.* **87**, 1057–1072 (2006).

52. V Agard, K Emanuel, Clausius–clapeyron scaling of peak cape in continental convective storm environments. *J. Atmospheric Sci.* **74**, 3043–3054 (2017).

53. K Emanuel, On the physics of high cape. *J. Atmospheric Sci.* **80**, 2669–2683 (2023).

54. AT LaFleur, RL Tanamachi, DT Dawson, DD Turner, Factors affecting the rapid recovery of cape on 31 march 2016 during vortex-southeast. *Mon. Weather. Rev.* **151**, 1459–1477 (2023).

55. P Tuckman, V Agard, K Emanuel, Evolution of convective energy and inhibition before instances of large cape. *Mon. Weather. Rev.* **151**, 321–338 (2023).

56. P Tuckman, K Emanuel, Origins of extreme cape around the world. *J. Geophys. Res. Atmospheres* **129**, e2024JD041833 (2024).

57. C Sauter, et al., Compound extreme hourly rainfall preconditioned by heatwaves most likely in the mid-latitudes. *Weather. Clim. Extrem.* **40**, 100563 (2023).

58. C Sauter, JL Catto, H Fowler, S Westra, CJ White, Compounding heatwave-extreme rainfall events driven by fronts, high moisture, and atmospheric instability. *J. Geophys. Res. Atmospheres* **128**, e2023JD038761 (2023).

59. NOAA’s National Weather Service, NOAA’s National Weather Service - Glossary (2025) Available at <https://forecast.weather.gov/glossary.php?word=cape>. Accessed 07 January 2025.

60. E Neal, CS Huang, N Nakamura, The 2021 pacific northwest heat wave and associated blocking: Meteorology and the role of an upstream cyclone as a diabatic source of wave activity. *Geophys. Res. Lett.* **49**, e2021GL097699 (2022).

61. TN Carlson, SG Benjamin, GS Forbes, YF Li, Elevated mixed layers in the regional severe storm environment: Conceptual model and case studies. *Mon. Weather. Rev.* **111**, 1453–1474 (1983).

62. FP Colby Jr, Convective inhibition as a predictor of convection during ave-sesame ii. *Mon. Weather. Rev.* **112**, 2239–2252 (1984).

63. BZ Ribeiro, LF Bosart, Elevated mixed layers and associated severe thunderstorm environments in South and North Americas. *Mon. Weather. Rev.* **146**, 3–28 (2018).

64. F Li, DR Chavas, KA Reed, DT Dawson II, Climatology of severe local storm environments and synoptic-scale features over north america in era5 reanalysis and cam6 simulation. *J. Clim.* **33**, 8339–8365 (2020).

65. F Li, DR Chavas, KA Reed, N Rosenbloom, DT Dawson II, The role of elevated terrain and the gulf of mexico in the production of severe local storm environments over north america. *J. Clim.* **34**, 7799–7819 (2021).

66. MS Andrews, et al., Climatology of the elevated mixed layer over the contiguous united states and northern mexico using era5: 1979–2021. *J. Clim.* **37**, 1833–1851 (2024).

67. EN Rasmussen, DO Blanchard, A baseline climatology of sounding-derived supercell and tornado forecast parameters. *Weather. Forecast.* **13**, 1148–1164 (1998).

68. M Taszarek, JT Allen, T Púčik, KA Hoogewind, HE Brooks, Severe convective storms across Europe and the United States. Part II: ERA5 environments associated with lightning, large hail, severe wind, and tornadoes. *J. Clim.* **33**, 10263–10286 (2020).

69. TM Weckwerth, DB Parsons, A review of convection initiation and motivation for ihop_2002. *Mon. weather review* **134**, 5–22 (2006).

70. JH Marsham, SB Trier, TM Weckwerth, JW Wilson, Observations of elevated convection initiation leading to a surface-based squall line during 13 june ihop_2002. *Mon. Weather. Rev.* **139**, 247–271 (2011).

71. YH Kuo, JD Neelin, Conditions for convective deep inflow. *Geophys. Res. Lett.* **49**, e2022GL100552 (2022).

72. S Pfahl, H Wernli, Quantifying the relevance of atmospheric blocking for co-located temperature extremes in the northern hemisphere on (sub-) daily time scales. *Geophys. Res. Lett.* **39** (2012).

73. M Bieli, S Pfahl, H Wernli, A lagrangian investigation of hot and cold temperature extremes in europe. *Q. J. Royal Meteorol. Soc.* **141**, 98–108 (2015).

74. M Röthlisberger, L Papritz, Quantifying the physical processes leading to atmospheric hot extremes at a global scale. *Nat. Geosci.* **16**, 210–216 (2023).

75. KA McKinnon, IR Simpson, AP Williams, The pace of change of summertime temperature extremes. *Proc. Natl. Acad. Sci.* **121**, e2406143121 (2024).

76. T Tamarin-Brodsky, K Hodges, BJ Hoskins, TG Shepherd, Changes in northern hemisphere temperature variability shaped by regional warming patterns. *Nat. Geosci.* **13**, 414–421 (2020).

77. EM Fischer, SI Seneviratne, PL Vidale, D Lüthi, C Schär, Soil moisture–atmosphere interactions during the 2003 european summer heat wave. *J. Clim.* **20**, 5081–5099 (2007).

78. DG Miralles, AJ Teuling, CC Van Heerwaarden, J Vilà-Guerau de Arellano, Mega-heatwave temperatures due to combined soil desiccation and atmospheric heat accumulation. *Nat. geoscience* **7**, 345–349 (2014).

79. MJ Molina, JT Allen, On the moisture origins of tornadic thunderstorms. *J. Clim.* **32**, 4321–4346 (2019).

80. X Li, et al., Role of atmospheric resonance and land–atmosphere feedbacks as a precursor to the june 2021 pacific northwest heat dome event. *Proc. Natl. Acad. Sci.* **121**, e2315330121 (2024).

81. JM Peters, et al., The influence of shear on deep convection initiation, part i: Theory. *J. Atmospheric Sci.* **79**, 1669–1690 (2022).

82. JM Peters, et al., The influence of shear on deep convection initiation, part ii: Simulations. *J. Atmospheric Sci.* **79**, 1691–1711 (2022).

83. MW Moncrieff, C Liu, Convection initiation by density currents: Role of convergence, shear, and dynamical organization. *Mon. Weather. Rev.* **127**, 2455–2464 (1999).

84. JM Peters, DR Chavas, CY Su, H Morrison, BE Coffer, An analytic formula for entraining cape in midlatitude storm environments. *J. Atmospheric Sci.* **80**, 2165–2186 (2023).

85. K Rasmussen, R Houze Jr, Convective initiation near the Andes in subtropical South America. *Mon. Weather. Rev.* **144**, 2351–2374 (2016).

86. TC Nelson, J Marquis, JM Peters, K Friedrich, Environmental controls on simulated deep moist convection initiation occurring during relampago-cacti. *J. Atmospheric Sci.* **79**, 1941–1964 (2022).

87. PC Banacos, DM Schultz, The use of moisture flux convergence in forecasting convective initiation: Historical and operational perspectives. *Weather. Forecast.* **20**, 351–366 (2005).

88. CL Ziegler, TJ Lee, RA Pielke, Convective initiation at the dryline: A modeling study. *Mon. Weather. Rev.* **125**, 1001–1026 (1997).

89. LJ Bennett, KA Browning, AM Blyth, DJ Parker, PA Clark, A review of the initiation of precipitating convection in the united kingdom. *Q. J. Royal Meteorol. Soc. A journal atmospheric sciences, applied meteorology physical oceanography* **132**, 1001–1020 (2006).

90. JP Mulholland, CJ Nowotarski, JM Peters, H Morrison, ER Nielsen, How does vertical wind shear influence updraft characteristics and hydrometeor distributions in supercell thunderstorms? *Mon. Weather. Rev.* (2024).

91. JM Peters, DR Chavas, ZJ Lebo, CY Su, Cumulonimbus clouds convert a smaller fraction of cape into kinetic energy in a warmer atmosphere. *J. Atmospheric Sci.* **81**, 1943–1961 (2024).

92. P Kassomenos, A Paschalidou, S Lykoudis, I Koletsis, Temperature inversion characteristics in relation to synoptic circulation above athens, greece. *Environ. monitoring assessment* **186**, 3495–3502 (2014).

93. T Tamarin, Y Kaspi, The poleward shift of storm tracks under global warming: A lagrangian perspective. *Geophys. Res. Lett.* **44**, 10–666 (2017).

94. J Keune, DL Schumacher, DG Miralles, A unified framework to estimate the origins of atmospheric moisture and heat using lagrangian models. *Geosci. Model. Dev.* **15**, 1875–1898 (2022).

95. MREW Group, Elevation-dependent warming in mountain regions of the world. *Nat. climate change* **5**, 424–430 (2015).

96. MP Byrne, WR Boos, S Hu, Elevation-dependent warming: observations, models, and energetic mechanisms. *Weather. Clim. Dyn.* **5**, 763–777 (2024).

97. ND Mueller, et al., Cooling of us midwest summer temperature extremes from cropland intensification. *Nat. Clim. Chang.* **6**, 317–322 (2016).

98. ML Barnes, et al., A century of reforestation reduced anthropogenic warming in the eastern united states. *Earth’s Futur.* **12**, e2023EF003663 (2024).

99. T Tamarin-Brodsky, K Hodges, BJ Hoskins, TG Shepherd, A dynamical perspective on atmospheric temperature variability and its response to climate change. *J. Clim.* **32**, 1707–1724 (2019).

100. BH Tang, VA Gensini, CR Homeyer, Trends in united states large hail environments and observations. *NPJ Clim. Atmospheric Sci.* **2**, 45 (2019).

101. Q Jiang, DT Dawson II, F Li, DR Chavas, Classifying synoptic patterns driving tornadic storms and associated spatial trends in the united states. *npj Clim. Atmospheric Sci.* **8**, 7 (2025).

102. M Taszarek, JT Allen, HE Brooks, N Pilguy, B Czernecki, Differing trends in United States and European severe thunderstorm environments in a warming climate. *Bull. Am. Meteorol. society* **102**, E296–E322 (2021).

103. M Taszarek, JT Allen, M Marchio, HE Brooks, Global climatology and trends in convective environments from era5 and rawinsonde data. *NPJ climate atmospheric science* **4**, 1–11 (2021).

104. DM Romps, MSE Minus CAPE is the True Conserved Variable for an Adiabatically Lifted Parcel. *J. Atmospheric Sci.* **72**, 3639–3646 (2015).

105. JM Peters, DR Chavas, Evaluating the conservation of energy variables in simulations of deep moist convection. *J. Atmospheric Sci.* **78**, 3229–3246 (2021).

106. R Madden, F Robitaille, A comparison of the equivalent potential temperature and the static energy. *J. Atmospheric Sci.* **27**, 327–329 (1970).

107. AK Betts, Further comments on “a comparison of the equivalent potential temperature and the static energy”. *J. Atmospheric Sci.* **31**, 1713–1715 (1974).

108. AJ DeCaria, Relating static energy to potential temperature: A caution. *J. atmospheric sciences* **64**, 1410–1412 (2007).

109. EA Eltahir, JS Pal, Relationship between surface conditions and subsequent rainfall in convective storms. *J. Geophys. Res. Atmospheres* **101**, 26237–26245 (1996).

110. P O’Gorman, CJ Muller, How closely do changes in surface and column water vapor follow clausius–clapeyron scaling in climate change simulations? *Environ. Res. Lett.* **5**, 025207 (2010).

111. CA Doswell III, EN Rasmussen, The effect of neglecting the virtual temperature correction on CAPE calculations. *Weather. forecasting* **9**, 625–629 (1994).

112. C Lepore, R Abernathey, N Henderson, JT Allen, MK Tippett, Future Global Convective Environments in CMIP6 Models. *Earth’s Futur.* **9**, e2021EF002277 (2021).

113. J Chen, A Dai, Y Zhang, KL Rasmussen, Changes in convective available potential energy and convective inhibition under global warming. *J. Clim.* **33**, 2025–2050 (2020).

114. KA Emanuel, M Bister, Moist convective velocity and buoyancy scales. *J. atmospheric sciences* **53**, 3276–3285 (1996).

115. DM Romps, Clausius–clapeyron scaling of cape from analytical solutions to ice. *J. Atmospheric Sci.* **73**, 3719–3737 (2016).

116. Z Wang, EJ Moyer, Robust relationship between midlatitudes cape and moist static energy surplus in present and future simulations. *Geophys. Res. Lett.* **50**, e2023GL104163 (2023).

117. F Li, DR Chavas, Midlatitude continental cape is predictable from large-scale environmental parameters. *Geophys. Res. Lett.* **48**, e2020GL091799 (2021).

DRAFT